

# Maximum Likelihood Identification of Inertial Sensor Noise Model Parameters

Janosch Nikolic, *Student Member, IEEE*, Paul Furgale, *Member, IEEE*, Amir Melzer, *Member, IEEE*, and Roland Siegwart, *Fellow, IEEE*

**Abstract**—Accurate visual-inertial localization and mapping systems require accurate calibration and good sensor error models. To this end, we present a simple offline method to automatically determine the parameters of inertial sensor noise models. The proposed methodology identifies noise processes across a large range of strength and time-scales, for example, weak gyroscope bias fluctuations buried in broadband noise. This is accomplished with a classical maximum likelihood estimator, based on the integrated process (i.e., the angle, velocity, or position), rather than on the angular rate or acceleration as is standard in the literature. This trivial modification allows us to capture noise processes according to their effect on the integrated process, irrespective of their contribution to rate or acceleration noise. The cause of the noise is not discussed in this article. The method is tested on different classes of sensors by automatically identifying the parameters of a standard inertial sensor noise model. The results are analyzed qualitatively by comparing the model's Allan variance to the Allan variance computed directly from sensor data. A simulation that resembles one of the devices under test facilitates a quantitative analysis of the proposed estimator. Comparison with a competing, state-of-the-art method shows the advantages of the algorithm.

**Index Terms**—Sensor phenomena and characterization, maximum likelihood estimation, gyroscope and accelerometer noise model.

## I. INTRODUCTION

**I**NERTIAL sensors are employed in countless applications, ranging from consumer electronics to autonomous vehicles and unmanned aerial systems. Many different types of sensors are used, from low-cost, multi-axis microelectromechanical systems (MEMS) devices with a footprint below 20mm<sup>2</sup>, to ring laser gyroscopes (RLGs). In order to understand the characteristics of these sensors, both stochastic (“noise”) and deterministic (sensitivity, axes misalignment, etc.) errors have to be considered.

When inertial measurements are combined with data from other sensors, such as precise landmark observations from a

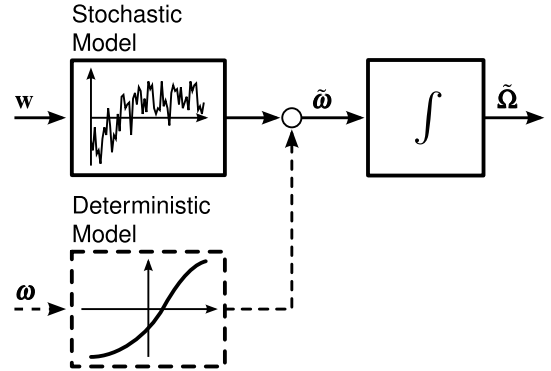


Fig. 1. Inertial sensor model with a deterministic and a random component. Here, the true angular rates  $\omega$  are corrupted with deterministic errors, for example a scale factor that varies with temperature, as well as non-deterministic errors, such as additive broadband noise. This report presents a method to identify noise processes according to their contribution to the angular increments  $\tilde{\Omega}$ .

camera system for example, an accurate model for the different sources of error in the inertial sensor data is vital. Such a model facilitates the optimal design of an estimator, and allows us to verify the proper operation of all software and hardware components.

A good sensor model often incorporates stochastic as well as deterministic components, as illustrated in Fig. 1. The stochastic part of the model includes errors such as broadband noise, or a slowly (randomly) varying bias, and describes them in a *probabilistic* sense. These errors can not be calibrated for, and limit the performance of the device fundamentally.

The instrumental noise figures are usually identified under static mechanical (i.e. non moving) and thermal conditions [1]. The stochastic model then provides an *upper bound* on the sensor performance, and crucial parameters for an estimator (i.e. noise densities).

This work focuses on how to identify such noise models automatically (for low-cost devices), since deriving a good noise model for an inertial sensor can be a difficult task for a non-expert. However, we also emphasise the importance of a good deterministic sensor model, since a stochastic model alone usually leads to over-confidence in the inertial data, especially when using uncalibrated sensors.

## A. Existing Methods

Section II reviews the most commonly used stochastic models for inertial sensors. The Allan variance (AV) [2] and

Manuscript received August 2, 2015; revised September 1, 2015; accepted September 1, 2015. Date of publication September 3, 2015; date of current version December 10, 2015. This work was supported in part by the Armassuisse Science and Technology under Grant 8003501880 and in part by the Commission for Technology and Innovation under Grant 13394.1 PFFLENM. The associate editor coordinating the review of this paper and approving it for publication was Dr. Amitava Chatterjee.

The authors are with the Autonomous Systems Laboratory, Swiss Federal Institute of Technology, Zurich CH-8092, Switzerland (e-mail: janosch.nikolic@mavt.ethz.ch; paul.furgale@mavt.ethz.ch; amir.melzer@mavt.ethz.ch; rsiegwart@ethz.ch).

Color versions of one or more of the figures in this paper are available online at <http://ieeexplore.ieee.org>.

Digital Object Identifier 10.1109/JSEN.2015.2476668

the non-parametric power spectral density (PSD), the classical tools to describe noise in inertial sensors, are revisited.

In practice, the noise model parameters are usually determined manually by “fitting” noise processes to estimates of the AV or the PSD. A detailed description of these procedures is provided, for example, in the Appendix of the IEEE standard 952-1997 [3]. These procedures are reliable, particularly those based on the Allan variance. Computing the sample based AV is standardized, and by the nature of the AV, the fitted noise models will be valid across the desired noise strength- and time-scales. The technical note [4], which is critical about applying classical automatic noise modelling techniques to inertial sensor data, presents convincing arguments for using this manual “AV method”.

However, these manual procedures require expertise to map the sample-based AV to parameters of a model which is useful for sensor fusion algorithms. The “Kalibr” toolbox<sup>1</sup> for spatial and temporal calibration of visual-inertial systems [5], for example, requires the user to specify the parameters of a particular inertial sensor noise model. An automatic method could eliminate the need for a manual identification of these noise model parameters.

Several methods were proposed for automatic identification of inertial sensor noise model parameters in the literature. The approach in [6] address the problem with a method that computes the theoretical covariance of the AV (given a model hypothesis), and then uses an optimal linear estimator to derive the parameters of a model whose AV matches the AV computed from measurement data. The method is intuitive and inherits the desirable properties of the manual AV method. It was developed in [6] for a model that incorporates white noise and a random walk process, and was tested on MEMS gyroscope and accelerometer data. In contrast to this method, the algorithm we propose does not aim to identify model parameters such that the model’s AV resembles the sample-based AV of the observed measurements.

The “Generalized Method of Wavelet Moments” (GMWM), proposed in [7], can be viewed as a generalization of this approach. Instead of the Allan variance, it uses a wavelet basis (“wavelet variance”), in which the sensor measurements are decomposed across different time-scales. Model parameters are then identified such that the model’s wavelet variance optimally matches the wavelet variance computed from the observed measurements. This state-of-the-art method was specifically developed for the identification of various noise processes in inertial sensors, and applied extensively for this purpose in [8]. An implementation of the method was provided by its developers, and we compare the performance of the method proposed in this article with the GMWM in Section IV.

[9] presents an innovation-based adaptive estimator for INS/GPS applications. A Kalman filter estimates the system state, while a maximum likelihood method uses a block of data to *independently* update the process and measurement covariance matrices. This results in a significant performance increase of their INS, and the method is suitable for

on-line applications. In contrast, our method provides a full maximum likelihood estimate of the noise model state and its parameters, and is intended for offline usage.

### B. Automatic Noise Model Parameter Identification

Section III develops a conceptually simple method to automatically identify the parameters of an inertial sensor noise model. A small change in the identification problem allows us to successfully apply *classical maximum likelihood* estimation to identify the parameters of the noise model. The method performs well for composite noise processes that span many strength- and time scales, such as weak MEMS gyroscope bias fluctuations buried in broadband noise.

In contrast to existing algorithms, the estimator we present works on the *integrated process* (i.e. the angle or velocity), rather than on the rate or acceleration measurements directly. The integrated process is an entirely different process, but arguably more relevant in sensor fusion applications, where information is often fused at an attitude, velocity, or position level. Noise processes which contribute to rate or acceleration noise only marginally may have a drastic effect on the integrated process, and vice versa. The proposed method exploits this by identifying the noise model parameters such that the resulting noise model is accurate for the integrated process, and captures noise processes even if their contribution to rate or acceleration noise is negligible. The algorithm is therefore called the “integrated maximum likelihood estimator”,  $ML_i$ . Model selection is not discussed.

### C. Deterministic Errors and Calibration

The deterministic part of the inertial sensor model captures non-random effects such as scale factor errors, axes misalignment, or frequency response. These non-idealities can, to some extent, be calibrated for, which often requires a per-device (factory) calibration across temperature, or on-line calibration mechanisms [10]. Different deterministic models of varying complexity are used in practice, depending on the type of sensor and application requirements. A simple model is used in Section IV to briefly quantify deterministic error sources. A dedicated experiment with a visual-inertial sensor setup highlights the uncomfortable fact that, particularly for uncalibrated low-cost devices, a sensor error model which is based on static sensor data alone, captured at constant temperature, does not capture inertial measurement errors well under *realistic operating conditions* (i.e. when the sensor undergoes motion, or the temperature varies).

For accurate visual-inertial localization and mapping systems, precise time-synchronization of cameras and inertial sensors is essential. Both software and hardware mechanisms exist to achieve this. We highlight the phase delay that a sensor internal decimation stage, a common feature in MEMS inertial sensors, can introduce. This is often overlooked in practice, but becomes apparent immediately when considering the entire “data acquisition process”, illustrated in Fig. 2. Sophisticated software-synchronization methods [5], [11] will automatically compensate for this, but hardware-synchronized systems will *not*.

<sup>1</sup>Kalibr is available at [www.github.com/ethz-asl/kalibr](http://www.github.com/ethz-asl/kalibr) (September 2015).

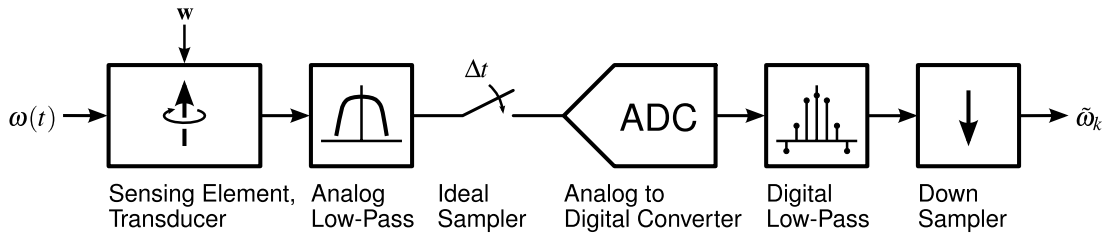


Fig. 2. Conceptual diagram of the data acquisition and pre-processing steps in inertial sensors. The sensing element captures the quantity of interest, here angular rate  $\omega(t)$ . Sensing electronics, often followed by an anti-aliasing mechanism, capture and condition the signal from the sensing element before it is sampled and digitized. The discrete-time rate or acceleration is then filtered with a digital low-pass filter and downsampled, *reducing noise* and introducing *delay*.

#### D. Experiments

Section IV tests the proposed method on sensor data from different device-classes, and verifies the identified noise models qualitatively using the classical Allan variance and the PSD as a reference. Additional tests show that the method is repeatable, and reliably captures the relevant noise processes. The accuracy of the proposed method is analysed quantitatively, using a simulation that resembles one of the devices under test. The method is also compared to a competing, state-of-the-art method (GMWM).

We show the limitations of purely stochastic sensor models, whose parameters were identified from static sensor data alone, in a dedicated experiment with a visual-inertial sensor system.

## II. STOCHASTIC SENSOR MODELS

The stochastic part of the sensor model captures errors which are considered random, and describes them in a probabilistic sense. Good examples of random errors are wideband “electronic noise”, originating from transducer and amplifier stages, or fluctuations in drive frequency that result in slowly varying, random gyroscope bias errors in MEMS devices [12]. Note that our aim here is not to link the noise model to a physical model of the sensor, but merely to derive generic, simple noise models which are suitable for *sensor fusion applications*, based on measurements.

This section summarizes the most important concepts in the description and analysis of noise processes in inertial sensor measurements, as far as they are relevant for the derivations that follow. The reader is referred to [13] for an excellent in-depth treatment of stochastic processes in general, and to [3] for a detailed collection of random processes that are useful to model noise in inertial sensors.

#### A. Spectral Density and Allan Variance

1) *Power Spectral Density*: The power spectral density is a standard tool for the description of stationary stochastic processes, and it is commonly used to characterize noise processes in gyroscopes and accelerometers [1], [3].

A number of *non-parametric* methods exist to compute the PSD from sampled data. A classical example is Welch’s method [14]. A good example for a parametric method is the identification of an autoregressive (AR) model by solving the Yule-Walker equations, based on sample covariance matrices.

Such classical methods struggle to capture weak processes with long correlation times, when they are buried deeply in broadband noise processes – a typical case in MEMS devices (see [4], [15] and Section IV-C). The Allan variance is a tool that is particularly well suited to handle exactly such cases.

2) *Allan Variance*: The Allan variance [2] addresses these issues and is an important tool in practice. Many manufacturers of inertial sensors include it in the device datasheet (see e.g. [16]), and engineers deduce key noise parameters from it. The reader is referred to [3] and the references therein for a more detailed treatment of the AV.

#### B. The Standard Noise Model

We now describe one of the most commonly used inertial sensor noise models – the same model whose parameters we identify in Section IV. The model combines “white noise”, capturing rapidly fluctuating noise processes, with an *exponentially time-correlated* process that captures slowly varying noise processes (biases). In engineering notation, we write:

$$z = x + v \quad (1a)$$

$$\dot{x} = -\frac{1}{\tau_b}x + w, \quad (1b)$$

where  $z$  is the modelled noise process, corrupting rate and acceleration measurements.  $v$  represents the white noise component of the model.  $x$  is the slowly varying (bias) process with correlation time  $\tau_b$ , “driven” by the white noise process  $w$ .  $w$  and  $v$  are independent, zero mean, white Gaussian noise processes of strength  $\sigma_b$  and  $\sigma_w$ . Formally:

$$E[w(t_1)w(t_2)] = \sigma_b^2 \delta(t_1 - t_2) \quad (2a)$$

$$E[v(t_1)v(t_2)] = \sigma_w^2 \delta(t_1 - t_2), \quad (2b)$$

where  $\delta(\cdot)$  denotes the Dirac delta function.

The model is popular due to its relatively large expressive power despite the small number of parameters  $\theta = \{\sigma_w, \sigma_b, \tau_b\}$ . It can be incorporated into state estimation frameworks efficiently due to its Gauss-Markov properties. It is for example used to model gyroscopes and accelerometers in a GPS aided INS [17], or in the context of a sun-sensor aided EKF attitude estimator in [18] (modelling noise in the gyroscopes, although with  $\frac{1}{\tau_b} = 0$ , i.e. a “pure” random walk bias model). [10], [19], [20] employ it in the context of visual-inertial simultaneous localization and mapping (SLAM).

TABLE I  
PARAMETERS OF THE STANDARD INERTIAL SENSOR NOISE  
MODEL (1a): TERMINOLOGY AND UNITS

Parameter	Description	Units
$\sigma_w$	(rate or acceleration) noise density, white noise density, angular or velocity random walk (ARW/VRW)	$\text{rad s}^{-1} \sqrt{\text{Hz}}^{-1}$ , $\text{m s}^{-2} \sqrt{\text{Hz}}^{-1}$
$\sigma_b$	bias diffusion, bias noise, random walk	$\text{rad s}^{-2} \sqrt{\text{Hz}}^{-1}$ , $\text{m s}^{-3} \sqrt{\text{Hz}}^{-1}$
$\tau_b$	bias correlation time	s, s

1) *Terminology*:  $\sigma_w$ , the strength of the rate or acceleration white noise process, is often termed “angular/velocity random walk” (ARW/VRW). IEEE standard [3] denotes  $\sigma_w$  as  $N$ , and device datasheets often refer to it simply as (rate or acceleration) noise density (see e.g. [16]).

$\sigma_b$ , the strength of the white noise process  $w$  that drives the bias fluctuations, is termed “bias diffusion” in this report. [3] uses  $K$  for this quantity when  $\frac{1}{\tau_b} = 0$ , and  $q_c$  otherwise. This is not equivalent to the “bias (in)stability”, which is used to parametrize flicker noise [21].  $\sigma_b$  is rarely reported in device datasheets. Table I summarizes the terminology.

2) *PSD and AV of the Standard Noise Model*: The PSD of the noise process  $z$  is the superposition of the PSD of the white noise process  $v$  and the time-correlated bias process  $x$ . The PSD of  $v$  is a constant,

$$\Psi_{vv}(f) = \sigma_w^2, \quad (3)$$

and the Allan variance of  $v$  is:

$$AV_v(\tau_A) = \frac{\sigma_w^2}{\tau_A}. \quad (4)$$

The PSD of the exponentially correlated bias process  $x$  (1b) is

$$\Psi_{xx}(f) = \frac{\sigma_b^2 \tau_b^2}{(2\pi \tau_b f)^2 + 1}. \quad (5)$$

For long correlation times,  $\lim_{\tau_b \rightarrow \infty} \Psi_{xx}(f) = \frac{\sigma_b^2}{(2\pi f)^2}$ . The AV of  $x$  is [3, Table B.1]:

$$AV_x(\tau_A) = \frac{\sigma_w^2 \tau_b^2}{\tau_A} \times \left[ 1 - \frac{\tau_b}{2\tau_A} \left( 3 - 4 \exp\left(-\frac{\tau_A}{\tau_b}\right) + \exp\left(-\frac{2\tau_A}{\tau_b}\right) \right) \right]. \quad (6)$$

For  $\tau_A \ll \tau_b$ ,  $AV_x$  is similar to the the AV of a random walk, and

$$AV_x(\tau_A) \approx \frac{\sigma_b^2}{3} \tau_A. \quad (7)$$

Figure 3 shows the power spectral density and the Allan deviation for the standard noise model, in log-log scale.

### Algorithm 1 Discrete-Time Equivalent of the Standard Noise Model (1a)

**init:**

$$\sigma_{wd}^2 \leftarrow \frac{1}{\Delta t} \sigma_w^2 \quad \triangleright \text{assuming } v \text{ is band-limited to } \frac{1}{2\Delta t}$$

$$\sigma_{bd}^2 \leftarrow \Delta t \sigma_b^2 \quad \triangleright \text{assuming } \tau_b \gg \Delta t$$

$$\Phi_d \leftarrow \exp\left(-\frac{1}{\tau_b} \Delta t\right)$$

$$x_0 \leftarrow \begin{cases} 0 & \text{if } \frac{1}{\tau_b} = 0 \text{ (by definition)} \\ \mathcal{N}\left(0, \frac{\sigma_b^2 \tau_b}{2}\right) & \text{otherwise} \end{cases}$$

**for**  $k \leftarrow 1$  **to**  $n$  **do**

$$w_k \leftarrow \mathcal{N}(0, \sigma_{bd}^2), v_k \leftarrow \mathcal{N}(0, \sigma_{wd}^2)$$

$$x_k \leftarrow \Phi_d x_{k-1} + w_k$$

$$z_k \leftarrow x_k + v_k$$

**end for**

3) *Discretization*: We briefly discuss the discretization of the standard noise model (1a), since it involves a simple, but crucial assumption. The discrete-time equivalent of the bias process (1b) is:

$$x_k = \exp\left(-\frac{1}{\tau_b} \Delta t\right) x_{k-1} + w_k \quad (8a)$$

$$E[w_k w_k] = -\frac{\sigma_b^2 \tau_b}{2} \left[ \exp\left(-\frac{2\Delta t}{\tau_b}\right) - 1 \right] = \sigma_{bd}^2, \quad (8b)$$

where  $w_k$  is a zero-mean, discrete-time white Gaussian noise process of strength  $\sigma_{bd}^2$ . If the bias correlation time is large compared to the sampling time ( $\tau_b \gg \Delta t$ ), then  $\sigma_{bd}^2 \approx \Delta t \sigma_b^2$ .

Discretization of the formal, infinite variance continuous-time “white noise” component  $v$  of the standard model requires more care. If one argues that  $v$  is ideally band-limited to  $\frac{1}{2\Delta t}$  before sampling, then

$$E[v_k v_k] = \frac{1}{\Delta t} \sigma_w^2 = \sigma_{wd}^2, \quad (9)$$

and

$$z_k = x_k + v_k, \quad (10)$$

where  $v_k$  is discrete-time, zero mean white Gaussian noise of strength  $\sigma_{wd}^2$ . The argument that  $v$  is integrated in-between samples would lead to the same result. If the measurements are simply subsampled without prior filtering, scaling  $\sigma_w^2$  with  $\frac{1}{\Delta t}$  is *not correct*. In other words, what should determine  $\sigma_{wd}^2$  is the *bandwidth* of  $v$  (determined by a correctly configured device-internal decimation stage, see Fig. 2), and not the sampling rate. Algorithm 1 summarizes the discrete-time equivalent implementation of the standard noise model.  $w \leftarrow \mathcal{N}(0, \sigma^2)$  denotes a zero-mean, normally distributed random variable with variance  $\sigma^2$ .

### C. Manual Identification

The parameters of the standard noise model (1a) can be directly read off of an Allan deviation plot under two conditions: a.) the noise can be approximated with the standard model, and b.) the noise is dominated by white noise

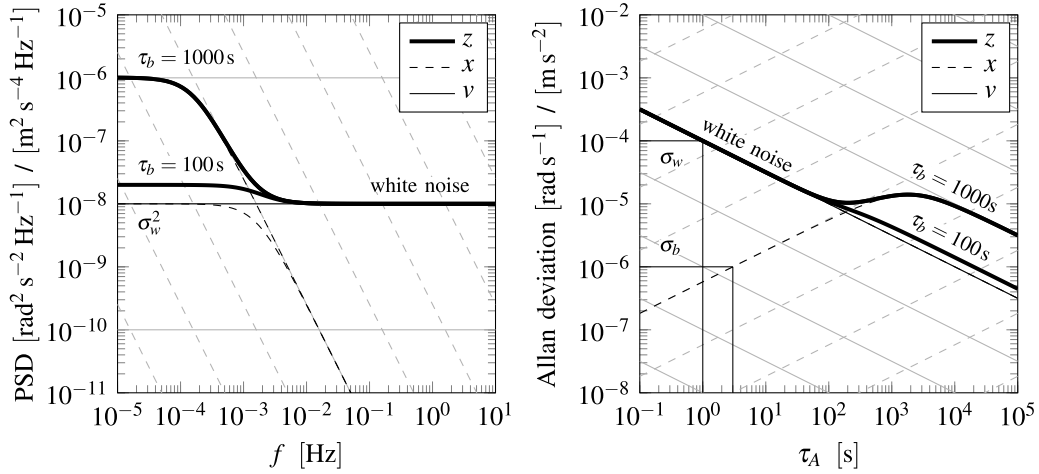


Fig. 3. Power spectral density (left) and Allan deviation (right) of the standard noise model (1a). Under certain conditions, the model parameters can be read off the sample based PSD and AV plots directly, as explained in Section II-C.

at  $\tau_A = 1\text{s}$ . If these conditions are met,  $\sigma_w$  corresponds approximately to the Allan deviation at  $\tau_A = 1\text{s}$  (see (4)).  $\sigma_b$  can be read off at  $\tau_A = 3\text{s}$ , as is clear from (7), and illustrated in Fig. 3. [22] describes manual procedures to identify other common noise processes, such as flicker noise (bias instability). The advantage of such manual procedures is that one can identify the characteristics of the noise process, and immediately see if the model fits the data well in terms of the Allan deviation.

### III. AUTOMATIC MODEL IDENTIFICATION

Obtaining the noise model parameters from the Allan variance or the PSD involves manually “fitting” graphs that correspond to known noise processes to the AV or the PSD that was computed from sensor data. This requires expertise. A method which can automatically identify the noise statistics will require less know-how, is less prone to error, and provides model parameters which are optimal with respect to probabilistic criteria.

The concept of *maximum likelihood* (ML) is well suited for problems that involve joint state, model, and noise statistics estimation, and is adopted here. ML estimators are asymptotically unbiased and attain the Cramér-Rao lower bound, even for problems that include the estimation of noise densities (discussed in detail in [23]).

#### A. The Integrated Noise Process

We propose one simple but crucial modification to the parameter identification problem. This modification allows us to apply classical maximum likelihood to identify typical noise processes in inertial sensors. Instead of estimating the parameters such that the model explains noise in the measurements directly (angular rate or acceleration), we identify the parameters such that noise in the *integrated* process is explained. This allows us to identify composite noise processes that span large strength- and time-scales, such as weak bias fluctuations “buried” deeply in broadband noise (a common case in MEMS inertial sensors, see [4] for a critical review of

existing automatic methods). While some noise processes contribute to noise power in acceleration or rate only marginally, they can have a drastic effect on the - arguable more relevant - integrated process (i.e. the velocity, position, or angle).

#### B. Augmented Noise Model

To identify the integrated noise process, the noise model is augmented with an integrator. This increases the dimension of the model by one, but only for identification purposes. The final noise model will have the desired structure again.

We will derive the likelihood function using a continuous-time formulation of the noise model, which allows us to think about the diffusion and the correlation of the bias processes in a natural way; in terms of noise power per unit of frequency and in seconds. Our attention is restricted to linear Gaussian noise models. We formally define the *augmented noise model* as follows:

$$\dot{\mathbf{x}}(t) = \mathbf{F}(\boldsymbol{\theta})\mathbf{x}(t) + \mathbf{G}\mathbf{w}(t) \quad (11a)$$

$$\bar{\mathbf{z}}(t_i) = \mathbf{H}\mathbf{x}(t_i). \quad (11b)$$

$\bar{\mathbf{z}}(t_i)$  denotes the integrated measurement process (sampled at time  $t_i$ ),  $\mathbf{x}$  denotes the state of the model,  $\mathbf{F}$  is the continuous-time “system matrix” (the desired noise model, augmented with an integrator), and  $\mathbf{w}$  is a continuous-time Gaussian “white noise” process of strength  $\mathbf{Q}$ ,  $E[\mathbf{w}(t_i)\mathbf{w}^T(t_j)] = \mathbf{Q}\delta(t_i - t_j)$ .  $\mathbf{H}$  denotes the 1-by- $p$  “measurement matrix”, and  $\mathbf{G}$  maps the driving noise  $\mathbf{w}$  on the state  $\mathbf{x}$ . The parameters of the model are summarized in  $\boldsymbol{\theta}$  and include, in particular, also the noise densities  $\mathbf{Q}$ . Note that the standard noise model (1a) can be cast into this form.

#### C. Maximum Likelihood Estimator

If the model parameters  $\boldsymbol{\theta}$  were known, estimating the state trajectory  $\mathbf{X}_m = \{\mathbf{x}(t_0), \mathbf{x}(t_1), \dots, \mathbf{x}(t_i)\}$  could be done efficiently due to the independence and the Gaussian assumption on  $\mathbf{w}$ . A Kalman filter [24] would in this case provide a sub-optimal solution for  $\mathbf{X}_m$ , and a smoother would give the optimal solution, given all measurements.

Jointly estimating the states  $\mathbf{X}_m$  and the parameters  $\theta$  is more complex, but a known problem as well. [25] and [26] apply the method of Expectation Maximization (EM) to parameter estimation in general linear systems. This involves a forward-backward Kalman smoothing step to obtain estimates for  $\mathbf{X}_m$  and its covariances, followed by a simple update of the model parameters. The two steps are then iterated.

However, this method is not applicable here, since we usually require the model to have a specific form (e.g.  $\mathbf{F}$  has a specific structure, or  $\mathbf{Q}$  is diagonal, etc.). We therefore resort to the classical “innovations likelihood” formulation as used by, for example, [27].

Due to the Markov and independence properties of the model, we can write the likelihood function in innovations form as

$$p(\bar{\mathbf{Z}}_m|\hat{\theta}) = \prod_{i=0}^m p(\bar{z}(t_i)|\bar{\mathbf{Z}}_{t_{i-1}}, \hat{\theta}), \quad (12)$$

where  $\bar{z}(t_i)$  denotes the value of the integrated noise process at time  $t_i$ , and  $\bar{\mathbf{Z}}_{t_i} = \{\bar{z}(t_0), \bar{z}(t_1), \dots, \bar{z}(t_i)\}$ . As we will see later,  $\bar{z}$  need not be uniformly sampled in time, hence  $\Delta t_i = t_i - t_{i-1}$  is not necessarily constant. For the  $\text{ML}_i$  log method, the measurement sequence is divided into  $m$  logarithmically increasing time-steps such that the entire sequence of  $n$  measurements is spanned.

Evaluation of (12) requires an expression for the conditional expectation of the mean and the covariance of each  $\bar{z}(t_i)$ . Given the model parameters  $\theta$ , they can be computed exactly. From time  $t_{i-1}$  to  $t_i$ ,  $\bar{z}(t)$  formally evolves as follows:

$$\begin{aligned} \bar{z}(t_i) = \mathbf{H} \times & \left[ \Phi(t_i, t_{i-1}) (\hat{\mathbf{x}}(t_{i-1}) - \Delta \mathbf{x}(t_{i-1})) \right. \\ & \left. + \int_{t_{i-1}}^{t_i} \Phi(t_i, s) \mathbf{w}(s) ds \right], \end{aligned} \quad (13)$$

where

$$\Phi(t_i, t_{i-1}) = \exp(\mathbf{F} \Delta t_i) \quad (14)$$

is the state transition matrix, and  $\Delta \mathbf{x}(t_{i-1}) = \mathbf{E}[\mathbf{x}(t_{i-1})|\bar{\mathbf{Z}}_{t_{i-1}}] - \mathbf{x}(t_{i-1})$  denotes the difference between the true state  $\mathbf{x}$  and our estimate  $\hat{\mathbf{x}}$  at time  $t_{i-1}$ .

Since the expectation of the stochastic integral in (13) is zero, the expected value of  $\bar{z}(t_i)$  is

$$\hat{\bar{z}}_i = \mathbf{E}[\bar{z}(t_i)|\bar{\mathbf{Z}}_{t_{i-1}}, \hat{\theta}] = \mathbf{H} \Phi(\Delta t_i) \hat{\mathbf{x}}(t_{i-1}). \quad (15)$$

For the covariance, we find

$$\begin{aligned} \mathbf{E}[\Delta \bar{z}(t_i)] &= \mathbf{H} \Phi(\Delta t_i) \mathbf{E}[\Delta \mathbf{x}(t_{i-1}) \Delta \mathbf{x}^T(t_{i-1})] \Phi^T(\Delta t_i) \mathbf{H}^T \\ &\quad + \mathbf{H} \int_{t_{i-1}}^{t_i} \Phi(t_i, s) \mathbf{E}[\mathbf{w}(s) \mathbf{w}^T(s)] \Phi^T(t_i, s) ds \mathbf{H}^T \\ &= \mathbf{H} (\mathbf{P}_{t_{i-1}|t_{i-1}} + \mathbf{Q}_d(\Delta t_i)) \mathbf{H}^T \\ &= B(t_i), \end{aligned} \quad (16)$$

where

$$\Delta \bar{z}(t_i) = \bar{z}(t_i) - \hat{\bar{z}}_i(t_i) \quad (17)$$

is the “prediction error”, and  $\mathbf{P}_{t_{i-1}|t_{i-1}} = \mathbf{E}[\Delta \mathbf{x}(t_{i-1}) \Delta \mathbf{x}^T(t_{i-1})]$  denotes the covariance of the state at

time  $t_{i-1}$ , given all  $\bar{\mathbf{Z}}_{t_{i-1}}$ .  $\mathbf{Q}_d(\Delta t_i)$ , the uncertainty in  $\mathbf{x}(t_i)$  introduced through  $\mathbf{w}$  since  $t_{i-1}$ , is written as

$$\mathbf{Q}_d(\Delta t_i) = \int_{t_{i-1}}^{t_i} \Phi(t_i, s) \mathbf{E}[\mathbf{w}(s) \mathbf{w}^T(s)] \Phi^T(t_i, s) ds. \quad (18)$$

Due to the properties of our model (linearity) and the assumptions on  $\mathbf{w}$ , all  $\Delta \mathbf{x}(t_i)$  and  $\Delta \bar{z}_i$  are normally distributed. The negative logarithm of the integrated process (12), the negative log-likelihood function, can therefore be written as

$$L(\hat{\theta}) = \frac{1}{2} \sum_{i=0}^m \left( \log B(t_i) + \Delta \bar{z}^2(t_i) B(t_i)^{-1} \right) + c, \quad (19)$$

where  $c$  captures terms that do not depend on  $\hat{\theta}$ .

The  $\hat{\theta}$  which minimizes (19) is then the maximum likelihood estimate of  $\theta$ . Minimization is performed iteratively, where each iteration requires a filtering step using the current estimate  $\hat{\theta}$ . Given  $\hat{\theta}$ , all terms in (19) can be computed recursively using the Kalman recursions. Additional methods are proposed in [27].

In classical state and parameter estimation problems,  $\log B(t_i)$  would be considered constant, and minimization of the log-likelihood would not depend on it. This is not the case here. Indeed,  $\log B(t_i)$  appears naturally, and penalizes “model complexity”.

#### D. Implementation

To obtain  $\bar{z}$ ,  $\mathbf{Z}_n$  (the  $n$  raw, i.e. not integrated rate or acceleration measurements) are integrated numerically:

$$\bar{z}(k \Delta t) = \bar{z}((k-1) \Delta t) + \Delta t z_{k-1}, \quad (20)$$

where  $z_{k-1}$  is the  $k$ -th raw measurement sample and  $\bar{z}(0) = 0$ . Integration is performed only once, but at the base sampling rate  $\Delta t$ .

The “sampling pattern”, the points in time  $t_i$  where  $\bar{z}$  is evaluated, is a design choice. We chose a logarithmic pattern ( $\Delta t_i$  increases logarithmically), but one could also argue for a uniform pattern where  $\Delta t_i$  is constant. A logarithmic pattern ensures that the noise characteristics of the sensor are well modelled at any time-scale, and that the computational complexity is reasonable for long experiments. Note that only the complexity of the numerical integration of  $\mathbf{Z}_n$  depends on the number of raw measurements  $n$ . One evaluation of the likelihood  $\bar{L}$  has complexity linear in  $m$ , the number of samples in the sampling pattern, and  $m \ll n$  for a logarithmic sampling pattern. For all our experiments, we chose  $m = 1000$ . Algorithm 2 summarizes the proposed method.

When computing  $\Phi(\Delta t_i, \hat{\theta})$  and  $\mathbf{Q}_d(\Delta t_i, \hat{\theta})$ , it is important to consider that the strengths and correlation times of noise processes in typical MEMS inertial sensors span several orders of magnitude. The broadband noise processes have short correlation times  $\ll 1$  s, while bias fluctuations often have correlation times larger than 100 s. The first-order approximation,  $\Phi \approx \mathbf{I} + \mathbf{F} \Delta t_i$ , is therefore not applicable here, since the integration time  $\Delta t_i$  can be long compared to the (broadband) dynamics in  $\mathbf{F}$ . For the same reason, the common approximation  $\mathbf{Q}_d \approx \Delta t_i \mathbf{Q} \mathbf{Q}^T$  is not valid. If the order of the model is small ( $\leq 2$ ), or the model has a special structure,

**Algorithm 2**  $ML_i$  Algorithm for Automatic Inertial Sensor Noise Model Parameter Identification. Corresponding Equations for Implementation are Given in Brackets

---

**input:** raw gyroscope or accelerometer measurements in  $\text{rad s}^{-1}$  or  $\text{m s}^{-2}$  (unfiltered, at sampling rate)  $\rightarrow \mathbf{Z}_n$

**procedure**  $ML_i(\text{model}, \hat{\boldsymbol{\theta}}_{\text{init}})$

integrate  $\mathbf{Z}_n$  numerically  $\rightarrow \bar{\mathbf{z}}(k \Delta t)$   $\triangleright$  (20)

select sampling pattern (e.g. “log”)  $\rightarrow \Delta t_i$   $\triangleright$  III-D

augment noise model with an integrator  $\rightarrow \mathbf{F}$

**minimize** log-likelihood  $\bar{L}$  numerically

**for**  $i \leftarrow 0$  **to**  $m$  **do**

    compute state transition  $\Phi(\hat{\boldsymbol{\theta}}, \Delta t_i)$   $\triangleright$  (14), (21)

    compute  $\mathbf{Q}_d(\hat{\boldsymbol{\theta}}, \Delta t_i)$   $\triangleright$  (21)

    compute prediction error  $\Delta \bar{\mathbf{z}}(t_i)$   $\triangleright$  (17)

    compute prediction error cov.  $B(t_i)$   $\triangleright$  (16)

**end for**

  compute log-likelihood  $\bar{L}$   $\triangleright$  (19)

**end**

  verify model (PSD, AV)  $\triangleright$  II-A

**return**  $\hat{\boldsymbol{\theta}}$

**end procedure**

---

$\Phi$  and  $\mathbf{Q}_d$  can be computed analytically. Otherwise,  $\hat{\Phi}(\Delta t_i, \hat{\boldsymbol{\theta}})$  can be approximated in many ways [28], and we use a scaling and squaring method to compute it.

To compute  $\mathbf{Q}_d$ , the variance induced into the model from  $t_{i-1}$  to  $t_i$  through the integral in (18), we make use of the following relationship from [29]:

$$\exp\left(\begin{bmatrix} -\mathbf{F} & \mathbf{G}\mathbf{Q}\mathbf{G}^T \\ \mathbf{0} & \mathbf{F}^T \end{bmatrix} \Delta t_i\right) = \begin{bmatrix} \mathbf{B} & \Phi(\Delta t_i)^{-1} \mathbf{Q}_d \\ \mathbf{0} & \Phi(\Delta t_i)^T \end{bmatrix}. \quad (21)$$

$\mathbf{Q}_d$  can then be extracted from the r.h.s. of (21). Important: The expression on the l.h.s. of (21) needs to be *balanced* before exponentiation (for long integration times  $\Delta t_i$ ).

#### IV. EXPERIMENTS

We now demonstrate that the proposed method accurately identifies noise models for different inertial sensors. Section IV-A describes the experimental setup. In Section IV-B, noise model parameters are automatically derived from real sensor data. The identified models are analysed qualitatively, using the classical Allan variance as a reference. The performance of the proposed method is then quantified in Section IV-C, using a simulation that resembles the behaviour of one of the devices under test. The method is then compared to a competing, state-of-the-art method for noise process identification in inertial sensors. Section IV-D assesses the validity of the models under real operating conditions.

##### A. Experimental Setup

To acquire sensor data for the experiments, the devices under test (DUTs) were attached to a rigid, non-moving object. Some of the experiments were conducted while the DUTs were mounted on a rate table, with all table axes and the temperature control equipment switched off entirely, to prevent spurious vibrations. Other sources of vibration,

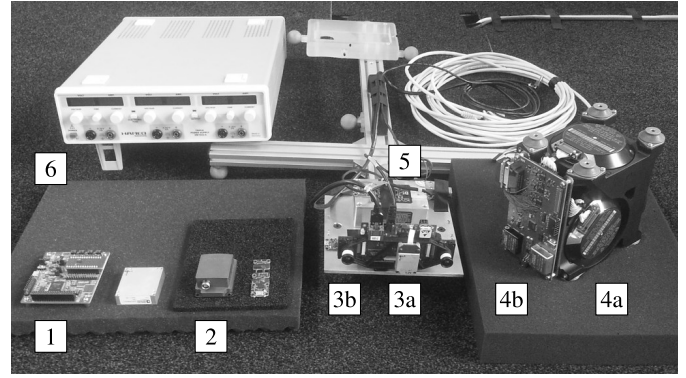


Fig. 4. Devices and laboratory equipment used during the experiments. 1. BMX055 MEMS IMU evaluation kit, 2. MTI100 MEMS IMU, 3. visual-inertial sensor unit (3a. ADIS16448, 3b. MPU9150), 4. inertial sensor assembly (4a. GG1320AN RLG, 4b. readout electronics), 5. DSP3000 FOG, 6. laboratory power supply used to power the devices under test.

such as the laboratory power supply that was used to power the DUTs, were separated from the setup to prevent vibrations.

Since even a small temperature change can cause a large variation in the sensor bias (up to  $100^\circ \text{h}^{-1} \text{K}^{-1}$  for low-cost MEMS devices), the experiments were conducted in a room with minimal variation in ambient temperature, although not temperature-controlled. Sensor data was only used for evaluation after a device warm-up time of  $\geq 1$  h. Temperature was monitored with three temperature sensors (type: MCP9804, accuracy:  $\pm 0.25^\circ \text{C}$ , resolution:  $0.0625^\circ \text{C}$ ), and recorded at a rate of 1 Hz. Sensor internal temperature, if available, was recorded along with the ambient temperature. Figure 4 shows the devices used for the experiments.

All sensors we tested have a digital interface, and a maximum sampling rate of  $\geq 100$  Hz. For a precise characterization of slower noise processes, the experiment durations were always  $> 10$  h. Raw data was recorded without any device external decimation (i.e. at sampling rate). Device-internal settings, such as range and bandwidth, were stored along with the raw data. IEEE standard 1554-2005 [30] provides additional useful recommendations on how to design experiments involving inertial sensors in general.

##### B. Models Derived From Real Sensor Data

We now apply the  $ML_i$  method, proposed in Section III, to identify noise models for real gyroscopes. We show that the automatically derived models are realistic by comparing their Allan variance and PSD – the classical tools in the analysis of inertial sensor noise characteristics – with the AV and non-parametric PSD computed directly from sensor data.

We employ the standard noise model (1a), with the addition of a fixed, but unknown “turn-on” bias. This is important since in many low-cost MEMS gyroscopes, the turn-on bias (in the order of  $1^\circ \text{s}^{-1}$ ) is much larger than the random bias variations that occur during operation. An alternative would be to remove the sample mean from the raw data prior to processing, as it is done in [7].

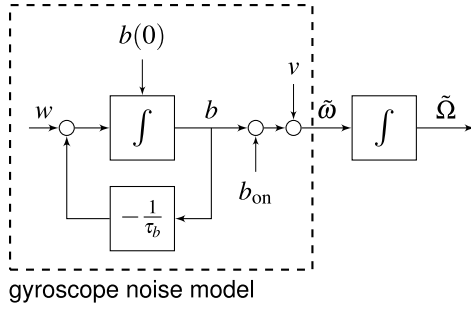


Fig. 5. Block diagram of the standard gyroscope sensor noise model for a single sensor axis (22a), derived from the standard model (1a).  $\tilde{\omega}$  denotes the measured angular rate,  $b$  the slowly fluctuating gyroscope bias,  $b_{\text{on}}$  a fixed but unknown turn-on bias, and  $w$  and  $v$  are white Gaussian noise processes.

For our gyroscope at rest, we therefore derive the following model from the standard noise model:

$$\tilde{\omega}(t) = b(t) + v(t) + b_{\text{on}} \quad (22a)$$

$$\dot{b}(t) = -\frac{1}{\tau_b} b(t) + w(t), \quad (22b)$$

where  $\tilde{\omega}$  denotes the measured angular rate,  $b$  is the sensor bias, and  $b_{\text{on}}$  models the unknown turn-on gyroscope bias.  $v$  and  $w$  are white Gaussian noise process of strength  $\sigma_w^2$  and  $\sigma_b^2$ , respectively, modelling broadband noise and driving bias fluctuations. Except for the turn-on bias  $b_{\text{on}}$ , the model is identical with the standard model. Figure 5 presents the gyroscope model as a block diagram.

This model can be cast in the *standard integrated form* (11a) as follows:

$$\dot{\mathbf{x}}(t) = \begin{bmatrix} -\frac{1}{\tau_b} & 0 & 0 \\ 0 & 0 & 0 \\ 1 & 1 & 0 \end{bmatrix} \mathbf{x}(t) + \begin{bmatrix} 0 & 1 \\ 0 & 0 \\ 1 & 0 \end{bmatrix} \mathbf{w}(t) \quad (23a)$$

$$\bar{\mathbf{z}}(t) = \begin{bmatrix} 0 & 0 & 1 \end{bmatrix} \mathbf{x}(t), \quad (23b)$$

where  $\bar{\mathbf{z}}$  corresponds to the integrated rate measurement (i.e. the angle  $\tilde{\Omega}$ ),  $\mathbf{x} = [b \ b_{\text{on}} \ \tilde{\Omega}]^T$ , and  $\mathbf{w} = [v \ w]^T$ . The model parameters are  $\theta = \{\sigma_w, \sigma_b, -\frac{1}{\tau_b}\}$ .  $b_{\text{on}}$ , the turn-on bias, is a nuisance parameter.

1) *Long Term Experiment*: We now apply the proposed integrated maximum likelihood estimator ( $\text{ML}_i$ ) to  $> 100$  h of data captured with the  $z$ -gyroscope of a BMX055 MEMS inertial measurement unit (IMU) from Bosch [31]. At a sampling rate of 400 Hz, this amounts to approximately  $n = 150$  M samples. The number of samples at which the integrated process is evaluated,  $m$ , is set to 1000. The model parameters are coarsely *initialized* to

$$\hat{\sigma}_b = 0 \quad (24a)$$

$$-\frac{1}{\hat{\tau}_b} = 0 \quad (24b)$$

$$\hat{\sigma}_w = \left[ \frac{1}{n} \sum_{k=0}^{n-1} (z_k - \mu_z)^2 \Delta t \right]^{\frac{1}{2}}, \quad (24c)$$

where  $\mu_z$  is the sample mean of  $\mathbf{Z}_n$ . In other words, the broadband noise strength is initialized with the

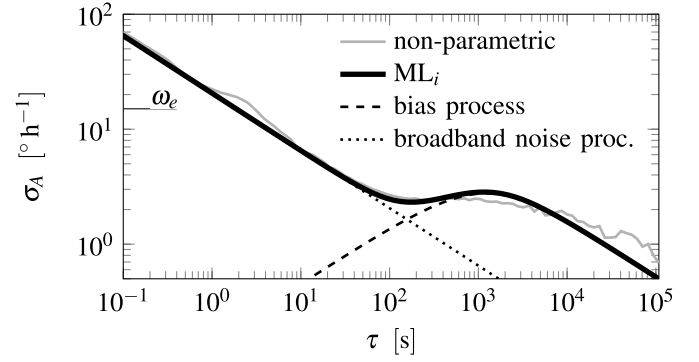


Fig. 6. Allan deviation of the BMX055  $z$ -gyroscope. Gray: non-parametric (sample) Allan deviation. Black (solid): Allan deviation corresponding to the automatically identified noise model (22a). It consists of a broadband noise component (dotted), and an exponentially time-correlated bias process (dashed). The earth's rotational rate  $\omega_e$  is shown for reference.

continuous-time equivalent of the sample standard deviation of the measurements, and the initial strength of the bias process is set to zero. The same initialization procedure was used for all experiments.

Figure 6 shows the results. The non-parametric standard Allan deviation, computed directly from  $\mathbf{Z}_n$ , is shown in gray. The Allan deviation corresponding to the identified model was computed analytically, and is shown in black (solid). It consists of the white noise process  $v$  (dotted), and the exponentially time-correlated bias process  $b$  (dashed).

Qualitatively, the model captures the noise characteristics at any time-scale  $> 0.1$  s. The model does not have enough expressive power to capture the non-white process visible at  $\tau \approx 2$  s, in addition to the slow bias variations at  $\tau > 1000$  s. Identification of the integrated noise process ensures that the processes which are most relevant for *angle noise power* are captured, even if they cause less rate noise power.

Note that the bias diffusion parameter  $\sigma_b$  is exceptionally small for a low-cost MEMS gyroscope (no other sensor from this class showed a better bias stability in our tests). This means that the bias fluctuations are “buried” particularly deeply in the broadband noise floor in this device. We found that the  $x$  and  $y$  gyroscopes of the BMX055 (not shown) perform worse than the  $z$  axis (in terms of noise), due to a different, out-of-plane implementation. Table II summarizes the results.

*Remark*: Given the model parameters, we can compute the rate noise power generated by the band-limited white noise and the bias noise process. Assuming a bandwidth of 47 Hz, broadband noise accounts for  $2 \cdot 47 \text{ Hz} \cdot (9.97 \times 10^{-5} \text{ rad s}^{-1} \sqrt{\text{Hz}}^{-1})^2 = 9.35 \times 10^{-7} \text{ rad}^2 \text{ s}^{-2}$ , or  $0.0554^\circ \text{ s}^{-1}$  RMS. The bias fluctuations account for only  $\frac{\sigma_b^2 \tau_b}{2} = 4.76 \times 10^{-10} \text{ rad}^2 \text{ s}^{-2}$ , or  $0.0012^\circ \text{ s}^{-1}$  RMS rate noise. This corresponds to a broadband to bias rate noise power ratio of  $\approx 2000 : 1$ , or 33 dB.

2) *Repeatability*: To confirm that the proposed method is repeatable, we applied it to ten datasets from the same device. The duration of each dataset is 12 h.

Figure 7 shows the results. The sample based Allan deviations are shown in gray, and those corresponding to the



TABLE II  
ML<sub>i</sub> ESTIMATOR RESULTS FOR THE LONG TERM EXPERIMENT  
WITH THE BMX055 z-GYROSCOPE

Parameter	Value	Unit
Experiment		
Device	BMX055 z-gyro	–
Sampling Rate	400	Hz
Device-Internal LPF	47	Hz
Experiment Duration	120	h
Model Parameters (ML <sub>i</sub> )		
White Noise Strength	$\sigma_w$ 20.57	$^{\circ} \text{h}^{-1} \sqrt{\text{Hz}}^{-1}$
Bias Diffusion	$\sigma_b$ $1.20 \times 10^{-6}$	$\text{rad s}^{-2} \sqrt{\text{Hz}}^{-1}$
Bias Correlation Time	$\tau_b$ 659.02	s

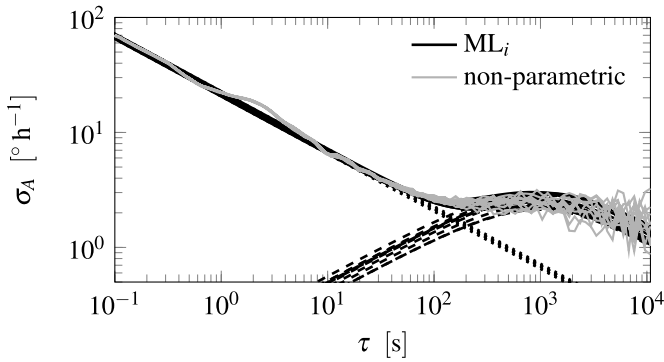


Fig. 7. Repeatability: Allan deviations of ten 12h datasets captured with the z-gyroscope of the BMX055 IMU. Gray: non-parametric estimates of the Allan deviations. Black: Allan deviations corresponding to the models that were automatically identified using ML<sub>i</sub>.

identified models are shown in black (solid). Qualitatively, the resulting models have similar characteristics across the entire time-scale. The flickering tendency at long integration times can not be captured with the model. The estimates of the broadband noise strength ( $\sigma_w$ ) are more repeatable than the estimates of the parameters related to the slow bias fluctuations ( $\sigma_b$  and  $\tau_b$ ).

$\sigma_b$  and  $\tau_b$  are inherently more difficult to estimate, since the likelihood function has a “flatter optimum” with respect to these parameters, even for long observations. In other words, a larger range of parameters explains the long-term behaviour of the observed sample path well. The best point estimate is therefore more sensitive to the specific realization of the noise process that was observed. The sample-based Allan deviation also suffers from this, as Fig. 7 shows. Table III summarizes these results. Note that the statistics of the parameter estimates that are indicated are computed using estimation results from different datasets. ML<sub>i</sub> itself does not provide estimates of parameter uncertainties.

3) *Testing With Different Devices*: The proposed estimator was tested on different gyroscopes, again using the standard noise model (22a). Figure 8 shows the Allan deviation for one of the axes of each of the devices under test. For multi-axes devices, the axis which is perpendicular to the device footprint (typically z) is shown. This is important since for

TABLE III  
SUMMARY OF REPEATED EXPERIMENTS WITH THE BMX055  
z-GYROSCOPE, PROCESSED WITH ML<sub>i</sub>. THE STATISTICS  
ARE COMPUTED FROM TEN 12 h DATASETS

Model Parameter	Mean	Std. Dev.	Units
White Noise Strength	$\sigma_w$ 21.66	0.66	$^{\circ} \text{h}^{-1} \sqrt{\text{Hz}}^{-1}$
Bias Diffusion	$\sigma_b$ $1.26 \times 10^{-6}$	$0.15 \times 10^{-6}$	$\text{rad s}^{-2} \sqrt{\text{Hz}}^{-1}$
Bias Correlation Time	$\tau_b$ 530.51	73.90	s

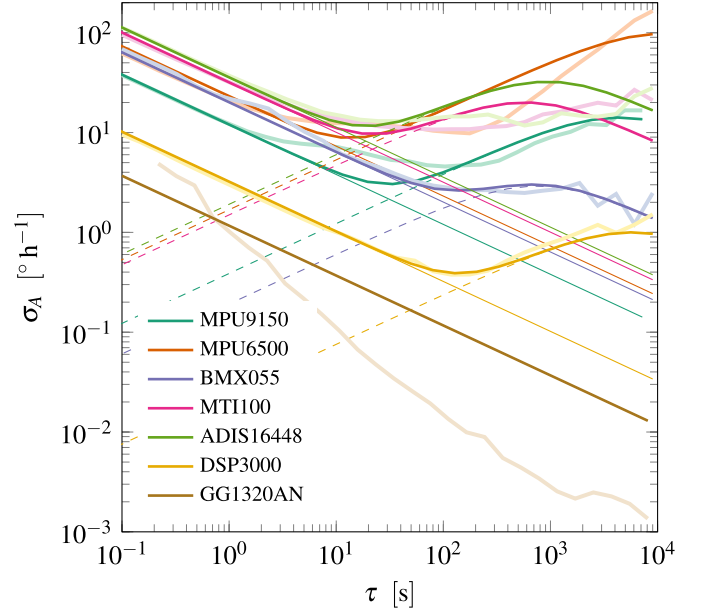


Fig. 8. Allan deviations of different gyroscopes under test (for multi-axes devices, only the gyroscope z-axis is shown). The sample based Allan deviations are shown in pastel, with an overlay of the Allan deviations that correspond to the identified standard noise models (ML<sub>i</sub>).

single chip MEMS devices, in contrast to e.g. the ADIS16448 or the MTI100, the performance between in-plane and out-of-plane axes often varies. Table IV lists the identified parameters (for all axes).

Qualitatively, in terms of the Allan deviation, ML<sub>i</sub> captures the noise processes well, considering the expressive power of the standard model. With one exception: the noise governing the GG1320AN dithered ring laser gyroscope [32] can not be adequately modelled with the standard noise model (since it is dominated by white *angle* noise at the time-scale of interest). This shows that the method can only be used for a fair comparison of inertial sensor noise performance if the assumed noise model structure is applicable.

4) *Noise Processes Near the Sampling Frequency*: Many MEMS inertial sensors have device-internal, digital filtering and sub-sampling stages that *decimate* the measurements before read-out, see Fig. 2. The decimation stage is often configurable, and allows the engineer to select a combination of bandwidth and output sampling rate. This has two important implications: a.) a significant *delay* can be introduced, depending on the selected bandwidth and filter architecture. An extreme bandwidth setting of 12 Hz, for example,

TABLE IV  
PARAMETERS OF THE STANDARD NOISE MODEL (1a), IDENTIFIED WITH  
THE PROPOSED  $ML_i$  ESTIMATOR, FOR DIFFERENT DEVICES

Device	Axis	$\sigma_w$ [rad s <sup>-1</sup> $\sqrt{\text{Hz}^{-1}}$ ]	$\sigma_b$ [rad s <sup>-2</sup> $\sqrt{\text{Hz}^{-1}}$ ]	$\tau_b$ [s]
MPU9150	x-gyro	$7.28 \times 10^{-5}$	$1.25 \times 10^{-5}$	$4.85 \times 10^3$
	y-gyro	$7.47 \times 10^{-5}$	$8.73 \times 10^{-6}$	$6.58 \times 10^3$
	z-gyro	$5.83 \times 10^{-5}$	$3.25 \times 10^{-6}$	$2.33 \times 10^3$
MPU6500	x-gyro	$1.42 \times 10^{-4}$	$5.66 \times 10^{-6}$	$1.68 \times 10^4$
	y-gyro	$1.08 \times 10^{-4}$	$1.09 \times 10^{-5}$	$5.99 \times 10^2$
	z-gyro	$1.12 \times 10^{-4}$	$1.42 \times 10^{-5}$	$5.94 \times 10^3$
BMX055	x-gyro	$1.24 \times 10^{-4}$	$1.65 \times 10^{-6}$	$5.37 \times 10^2$
	y-gyro	$1.99 \times 10^{-4}$	$2.41 \times 10^{-6}$	$2.44 \times 10^3$
	z-gyro	$9.97 \times 10^{-5}$	$1.20 \times 10^{-6}$	$6.59 \times 10^2$
MTI100	x-gyro	$1.49 \times 10^{-4}$	$2.78 \times 10^{-5}$	$1.49 \times 10^2$
	y-gyro	$2.16 \times 10^{-4}$	$1.06 \times 10^{-5}$	$2.05 \times 10^3$
	z-gyro	$1.54 \times 10^{-4}$	$1.26 \times 10^{-5}$	$3.11 \times 10^2$
DSP3000	—	$1.56 \times 10^{-5}$	$2.01 \times 10^{-7}$	$3.05 \times 10^3$
ADIS16448	x-gyro	$1.75 \times 10^{-4}$	$1.55 \times 10^{-5}$	$4.01 \times 10^2$
	y-gyro	$1.64 \times 10^{-4}$	$1.27 \times 10^{-5}$	$2.87 \times 10^2$
	z-gyro	$1.73 \times 10^{-4}$	$1.61 \times 10^{-5}$	$4.99 \times 10^2$

can introduce a delay  $> 30$  ms. If the inertial data is combined with e.g. precise 2D landmark observations from a camera system, this needs to be accounted for. b.) The decimation stage introduces additional dynamics in the noise processes (close to the sampling frequency). An automatic noise model parameter estimation mechanism that works on rate or acceleration directly will aim to model these dynamics – since it is designed to explain rate or acceleration noise power. As a result, the method may quickly fail to capture weak bias fluctuations, even though they contribute more significantly to noise in the integrated process. In contrast,  $ML_i$  copes well with such cases, since it tries to explain the *integrated process* itself.

Figure 9 shows the PSD of the BMX055 z-gyroscope measurements close to the sampling frequency. A non-parametric estimate of the PSD, computed using Welch’s method [14], is shown in gray for frequencies from 1 Hz to 200 Hz (half the sampling frequency). The effect of a decimation stage, with a cut-off frequency setting of 47 Hz, is clearly visible; it limits the bandwidth of the broadband noise. If required, these processes can be identified using any of the classical methods. Once the model parameters are identified, the exact PSD of the process generated by the model can be computed. The PSD corresponding to the identified model of order one and two are shown in black.

Since the dynamics of these processes are usually faster than the rate at which information from an aiding sensor, e.g. a camera, is incorporated, they are usually not part of an inertial sensor model.

### C. Simulations

This section uses simulated data to analyse the proposed estimator quantitatively. The simulation resembles, to some extent, the noise characteristics of one of the devices analysed in Section IV-B: the z-gyroscope of the BMX055 MEMS IMU.

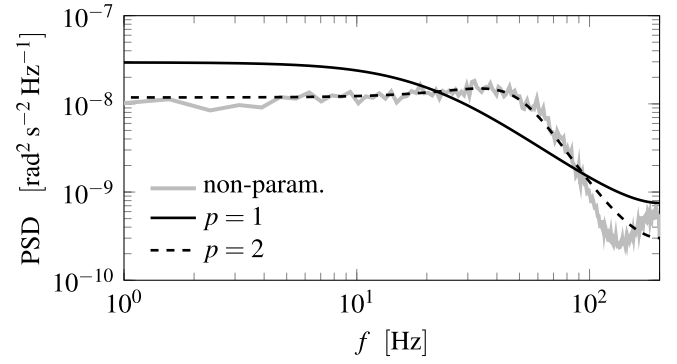


Fig. 9. Power spectral density (PSD) of the BMX055 z-gyroscope near the sampling frequency (double-sided density). The non-parametric PSD, computed using Welch’s method, is shown in gray. The PSD of the automatically identified models of order  $p = 1$  and  $p = 2$  are shown in black.

The standard model (22a) is used, with parameters drawn according to the values reported in Table III. In contrast to the experiments in the previous sections, we now have access to the true noise model parameters  $\theta$ .

1) *Comparison With Direct Methods:* Figure 10 shows the statistics of the bias diffusion strength  $\sigma_b$  (top) and the bias correlation time  $\tau_b$  (bottom) estimates, for different estimators. The bias diffusion strength  $\sigma_b$  was varied in order to emulate increasing levels of bias fluctuation, while  $\sigma_w$  and  $\tau_b$  were held constant. The lowest  $\sigma_b$  of  $1.15 \times 10^{-6} \text{ rad s}^{-2} \sqrt{\text{Hz}^{-1}}$  corresponds approximately to the bias diffusion of the BMX055 gyroscope (see Table III) – a small value for this class of sensors and this level of broadband noise.

For high levels of bias diffusion, all methods perform well, including classical maximum likelihood on uniformly sampled rate noise (ML uniform). Once the bias fluctuations approach realistic values, identification of the integrated (angle) noise process ( $ML_i$ ) has an advantage. The logarithmic sampling strategy of the  $ML_i$  log estimator, favouring models which represent the noise characteristics at any time-scale, leads to accurate estimates of the bias diffusion strength and the bias correlation time at all levels of bias diffusion. The characteristics of the broadband noise processes were estimated accurately in all configurations (not shown).

2) *Comparison With Other Methods:* We now compare the proposed estimator with the state-of-the-art “Generalized Method of Wavelet Moments” (GMWM), developed specifically for the identification of such noise processes [7], and applied extensively to inertial sensor noise modelling [8]. GMWM provides models which are accurate across all time-scales by decomposing the measurements in a wavelet basis. It can also be used to identify more complex noise processes, such as quantization noise and bias instability (flickering), something our method is not capable of.

GMWM requires the selection of a specific wavelet basis, and the choice has an influence on the resulting parameter estimates. Our method, on the other hand, requires the selection of a sampling pattern. The pattern also has an influence on the parameter estimates, since it will ultimately determine the time-scales at which the model is forced to represent the observed (integrated) noise process well.

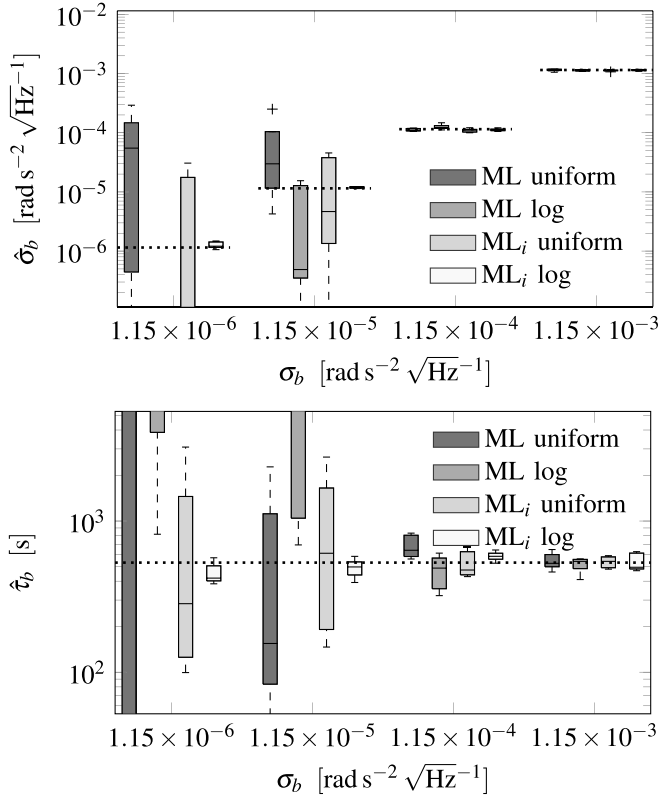


Fig. 10. Estimated sensor bias diffusion ( $\hat{\sigma}_b$ ) and correlation time ( $\hat{\tau}_b$ ) for classical (ML) and integrated (ML<sub>i</sub>) maximum likelihood methods, using uniform (uniform) and logarithmic (log) sampling schemes, for varying levels of bias diffusion.

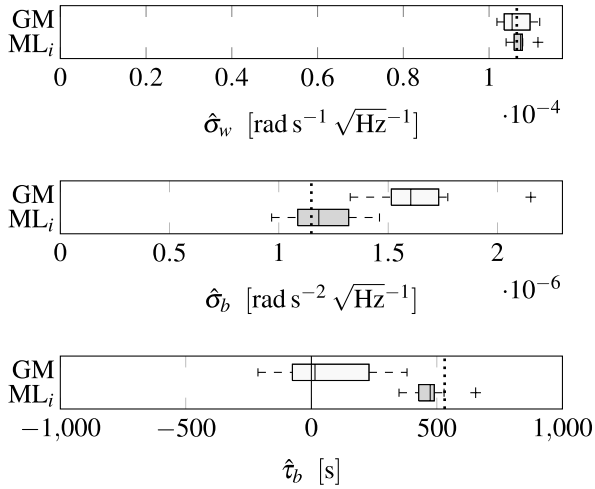


Fig. 11. Parameter estimates from two different methods: the generalized method of wavelet moments (GM) [7], [8], and integrated maximum likelihood (ML<sub>i</sub>). The standard model parameters were estimated for 10 synthetic datasets, each 12 h long. Ground truth is indicated with a dotted line.

Figure 11 shows a comparison of the two methods, again using a simulation of the standard model (22a) with parameters derived from Table III. Both methods were employed on ten simulated datasets with a length of 12 h each. The resulting estimates are shown in grey (ML<sub>i</sub>) and white (GMWM).<sup>2</sup>

<sup>2</sup>An implementation of GMWM [7] was provided by the “Geodetic Engineering Laboratory” (Ecole Polytechnique Fédérale de Lausanne).

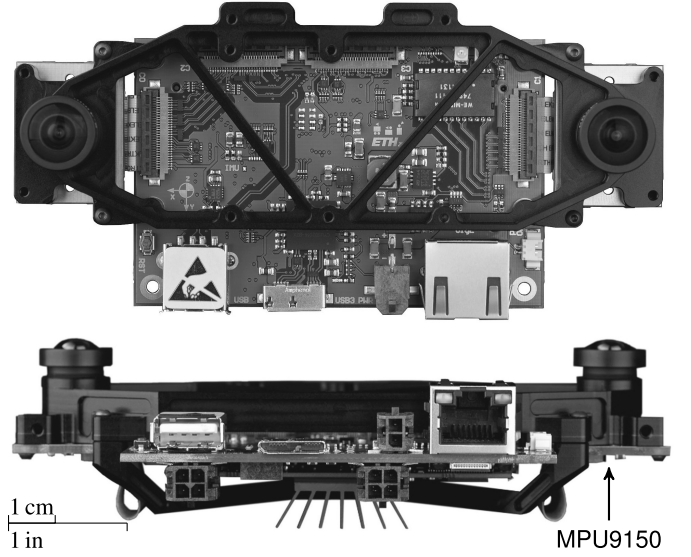


Fig. 12. Visual-inertial sensor unit [33] used for assessing inertial sensor performance under motion, in front of a visual calibration target. An MPU9150 MEMS IMU is located behind each of the cameras, and used for testing.

The broadband noise strength  $\sigma_w$  is estimated accurately by both methods. The bias diffusion  $\sigma_b$  is generally estimated less accurately, and the estimates provided by the GMWM appear slightly biased. The bias correlation time  $\tau_b$ , a difficult parameter to estimate for this noise process (see Section IV-C), is estimated to within approximately  $\pm 120$  s of  $\tau_b = 530$  s.

#### D. Device Characteristics Under Normal Operating Conditions

Two important questions remain unanswered:

- 1) Do the noise models still capture the sensor errors well enough under normal operating conditions, i.e. when the sensor is in motion?
- 2) Can we actually achieve the performance predicted by the noise model, with and without device calibration?

To address these questions, a series of experiments were conducted, with the aim to give a qualitative insight into the different sources of error in low-cost inertial sensors.

1) *Devices Under Motion:* We first conduct an experiment where the sensors undergo *arbitrary motion*. The experiment relies on our visual-inertial sensor unit [33], shown in Fig. 12. The unit incorporates several MEMS IMUs, synchronized and rigidly attached to two global-shutter CMOS camera sensors. We compare the integrated state of the unit (using gyroscopes and accelerometers) with pose estimates from the camera system. This then allows us to qualitatively evaluate whether the noise models are valid under these conditions, or not.

During the experiment, the visual-inertial sensor unit followed a smooth trajectory (hand-held) in front of a visual calibration target. Rate and acceleration were in the range of  $\pm 180^\circ \text{ s}^{-1}$  and  $\pm 2g$ . No shocks or vibrations were present, and device temperature was constant to within  $< 1.5^\circ\text{C}$ . The IMUs were sampled at 200 Hz, the cameras at 20 Hz.

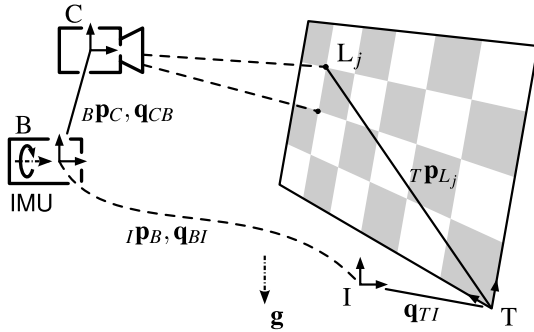


Fig. 13. Schematic overview of the experiment involving the visual-inertial sensor unit and the calibration target. Once the setup is accurately calibrated, errors in the (moving) inertial sensors can be quantified.

The cameras were calibrated intrinsically prior to the experiments, using Kalibr. Target observations with the camera system then provided a noisy, potentially biased through inaccuracies in camera in- and extrinsics, but *error-bounded* ground-truth for the orientation and the position of the sensor unit with respect to the target, at a rate of 20 Hz.

Figure 13 shows a schematic overview of the experimental setup. To make a precise statement about the accuracy of the inertial sensor data under motion, the following parameters have to be estimated:

$\mathbf{p}_B(t), \mathbf{q}_B(t), \mathbf{v}_B(t)$	Pose and velocity of the sensor units (body) frame $B$ , expressed in an inertial frame of reference $I$ . $B$ coincides with the input reference axes of the IMU.
$B\mathbf{p}_C, \mathbf{q}_{CB}$	Camera $C$ to IMU transformation.
$\mathbf{q}_{TI}$	The orientation of the calibration target $T$ with respect to the gravity vector $\mathbf{g}$ (two degrees of freedom).
$t_{BC}$	A fixed time-difference between the cameras and the IMUs (IMU internal delays).
$\mathbf{C}_I$	IMU intrinsic calibration parameters (scale factors, axes misalignment).
$\mathbf{b}_g(t), \mathbf{b}_a(t)$	Gyroscope and accelerometer biases.

All of these states and parameters were estimated using a classical, discrete-time maximum likelihood (batch) estimator.

The estimator incorporates all measurements (i.e. every sample from the gyroscope and the accelerometer, and all undistorted 2D camera observations of corners in the visual target). The states were estimated at each time-instance at which a camera frame was captured. The parameters, such as the camera to IMU extrinsics or the IMU calibration parameters, were assumed fixed but unknown, and estimated at the same time. Up to linearisation, and under the assumption that the sensor models that were used are correct, this estimator is asymptotically optimal. The details of the estimator are not discussed in this report.

Figure 14 shows the difference between the gyroscope integrated attitude, and the attitude which was estimated using only observations from the cameras. Following the “full batch” estimation, outlined above, the state of the system was fixed at  $t_0$  to the estimate from the full batch estimator (at  $t_0$ ). The initial covariances of the sensor biases were obtained from the

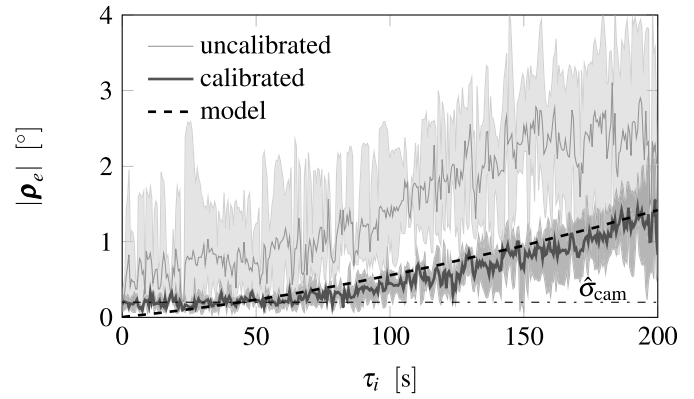


Fig. 14. Attitude error (RMS) for five experiments with the visual-inertial sensor unit in motion. Black (dashed): predicted square root of the integrated attitude error, computed using the automatically identified gyroscope noise models. Gray: differences between the integrated attitude (calibrated and uncalibrated) and the attitude estimated with the camera system.  $\hat{\sigma}_{\text{cam}}$ : approximate uncertainty in the transformed camera attitude estimates (determined from this figure).

respective elements of the inverse information matrix of the estimator [34]. The state was then integrated using only inertial measurements (from the gyroscopes and accelerometers). The orientation of the cameras with respect to the target (computed using the cameras only) was transformed using the estimated parameters of the camera-IMU extrinsics, time delay, and orientation of the target with respect to gravity. Shown in Fig. 14 is the square root of the variance of the rotation (magnitude) between the two frames.

Also shown is the uncertainty as predicted by the automatically identified IMU noise model (dashed). The variance of the model was computed numerically (to first order). The predicted uncertainty is composed of a.) an angular random walk component due to the white noise part of the model, b.) the integrated bias processes, and c.) uncertainty in the state (biases) of the model at  $t_0$ , the beginning of integration.

The square root of the variance of the integrated attitude for the *uncalibrated* device (averaged over five experiments) is larger than predicted by the model. This indicates that the pure noise model is too optimistic, and does not account for errors that are introduced once the uncalibrated device is in motion. This is not surprising, considering the scale of the deterministic errors that are present in a sensor of this class. Gyroscope axes misalignment angles, for example, were estimated to be in the order of  $0.5^\circ$ . In other words, even a small rate on one axis may cause an almost instantaneous apparent “bias” on an other axis which, considering only the static noise model, would be very unlikely to occur. Clearly, the errors introduced through deterministic errors depend on the motion.

Also shown are the results from the same experiment, but incorporating IMU intrinsic calibration terms in the integrator (scale factors and misalignment). This leads to a better agreement between predicted (model) variance and measured variance. Indeed, the performance of the gyroscopes are in the order of the performance predicted by the static noise model.

2) *Temperature*: The results presented above suggest that IMU intrinsic calibration reduces the deterministic errors in the

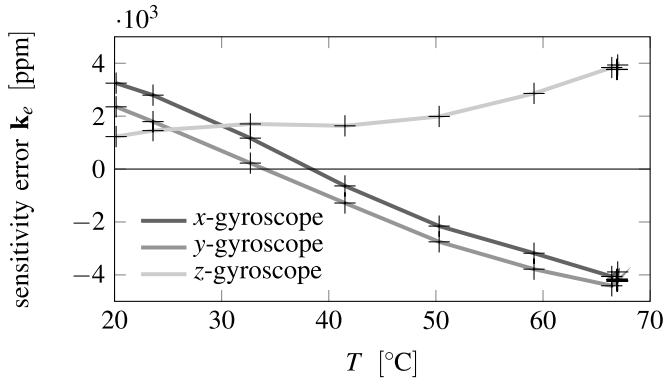


Fig. 15. Estimated sensitivity error of the BMX055 gyroscopes as a function of temperature.

inertial data. Indeed, a low-cost MEMS IMU IC *outperformed* a factory-calibrated IMU that consists of several single-axis (MEMS) gyroscopes and accelerometers – simply due to *better noise performance*. It is crucial to note, however, that the experiments were conducted at constant temperature (and no temperature-cycles in-between experiments), and with smooth motion (no vibrations). In practice temperature may vary rapidly, not only due to changes in ambient temperature, but also due to device internal temperature changes.

Temperature plays an important role in MEMS inertial sensors, and its influence can quickly invalidate the noise model. We show this with the example sensor sensitivity changes as a function of temperature. To this end, we conducted experiments on a three-axis rate table with a temperature chamber [35]. Temperature was ramped from room temperature to approximately 65°C, while 42-element motion profiles (based on the classical 18-element sequence proposed in [36]) were executed repeatedly. The total experiment duration is below 1 h per three axis device (either angular rate or acceleration, since the motion profile is not the same). Extrinsic (IMU input reference axes to rate table) and IMU intrinsic calibration parameters were jointly estimated.

Figure 15 shows the change in the scale factor (the sensitivity) of one of the MEMS gyroscopes we tested [31]. This particular device showed a change in the scale factor with temperature of up to 150ppmK<sup>-1</sup>. In the same sensor, a gyroscope bias temperature sensitivity of up to 40° h<sup>-1</sup> K<sup>-1</sup> was registered (not shown). For typical operating conditions, such temperature induced bias changes can easily outweigh the random bias variations captured with the noise model. This is one of the reasons why low-cost inertial sensor noise model parameters are often considered “tuning parameters”. It is also apparent that device calibration, if performed at constant temperature, is *only valid for this temperature range*, and may even increase error if applied at a different operating temperature. [10] addresses this (in a visual-inertial SLAM context), by tracking IMU intrinsic model parameters (scale factors, misalignment, and g-sensitivity) *on-line*.

## V. CONCLUSION

This report presented a method to automatically identify the parameters of inertial sensor noise models. By identifying

noise processes according to their contribution to the integrated process, processes that span many time- and strength scales were easily captured with a classical maximum likelihood estimator. The resulting models are accurate at an attitude, velocity, or position level, and are therefore appropriate for usage in sensor fusion applications.

A qualitative analysis of the method on different devices showed that it performs well on real sensor data. An experiment involving a visual-inertial sensor unit demonstrated the usefulness of the method for *practical applications*. And a quantitative analysis, based on simulated data, highlighted the capability of the method to accurately characterize challenging composite noise processes.

We also concluded that the derived error models are too optimistic for uncalibrated devices under real operating conditions. A useful extension of this work would therefore be to automatically tune noise model parameters *under these conditions*. In a visual-inertial estimation context, for example, a joint optimization of deterministic and stochastic model parameters is possible – in principle.

## ACKNOWLEDGMENT

The authors wish to express their gratitude to Joern Rehder, Michael Burri, Pascal Gohl, and Stefan Leutenegger, amongst others, for their commitment and their tireless engineering efforts that lead to the visual-inertial sensor unit which facilitated our experiments. They thank Gabriel Agamennoni and Simon Lynen (ETH Zürich) for their scientific contributions. They thank Joel Hesch, Renzo de Nardi, and Johnny Lee (Google) for supporting us with their expertise and equipment, and the Geodetic Engineering Laboratory at EPFL for providing a well documented implementation of the GMWM.

## REFERENCES

- [1] R. O. Allen and D. H. Chang, “Performance testing of the Systron Donner quartz gyro (QRS11-100-420),” Jet Propuls. Lab., Pasadena, CA, USA, Tech. Rep. EM 343-1297, 1993.
- [2] D. W. Allan, “Statistics of atomic frequency standards,” *Proc. IEEE*, vol. 54, no. 2, pp. 221–230, Feb. 1966.
- [3] *IEEE Standard Specification Format Guide and Test Procedure for Single-Axis Interferometric Fiber Optic Gyros*, IEEE Standard 952-1997, 1998.
- [4] Y. Yuksel and H. Kaygisiz. (2012). *Stochastic Errors of Low Cost MEMS Inertial Units*. [Online]. Available: <http://www.instk.org/>
- [5] P. Furgale, J. Rehder, and R. Siegwart, “Unified temporal and spatial calibration for multi-sensor systems,” in *Proc. IEEE/RSJ Int. Conf. Intell. Robots Syst. (IROS)*, Nov. 2013, pp. 1280–1286.
- [6] R. J. Vaccaro and A. S. Zaki, “Statistical modeling of rate gyros,” *IEEE Trans. Instrum. Meas.*, vol. 61, no. 3, pp. 673–684, Mar. 2012.
- [7] S. Guerrier, J. Skaloud, Y. Stebler, and M.-P. Victoria-Feser, “Wavelet-variance-based estimation for composite stochastic processes,” *J. Amer. Statist. Assoc.*, vol. 108, no. 503, pp. 1021–1030, 2013.
- [8] Y. Stebler, S. Guerrier, J. Skaloud, and M.-P. Victoria-Feser, “Generalized method of wavelet moments for inertial navigation filter design,” *IEEE Trans. Aerosp. Electron. Syst.*, vol. 50, no. 3, pp. 2269–2283, Jul. 2014.
- [9] A. H. Mohamed and K. P. Schwarz, “Adaptive Kalman filtering for INS/GPS,” *J. Geodesy*, vol. 73, no. 4, pp. 193–203, 1999.
- [10] M. Li, H. Yu, X. Zheng, and A. I. Mourikis, “High-fidelity sensor modeling and self-calibration in vision-aided inertial navigation,” in *Proc. IEEE Int. Conf. Robot. Autom. (ICRA)*, May/Jun. 2014, pp. 409–416.
- [11] M. Li and A. I. Mourikis, “Online temporal calibration for camera-IMU systems: Theory and algorithms,” *Int. J. Robot. Res.*, vol. 33, no. 7, pp. 947–964, 2014.

- [12] V. Kempe, *Inertial MEMS: Principles and Practice*. Cambridge, U.K.: Cambridge Univ. Press, 2011.
- [13] P. S. Maybeck, *Stochastic Models, Estimation and Control*. New York, NY, USA: Academic, 1979.
- [14] P. D. Welch, "The use of fast fourier transform for the estimation of power spectra: A method based on time averaging over short, modified periodograms," *IEEE Trans. Audio Electroacoust.*, vol. 15, no. 2, pp. 70–73, Jun. 1967.
- [15] Y. Yuksel, N. El-Sheimy, and A. Noureldin, "Error modeling and characterization of environmental effects for low cost inertial MEMS units," in *Proc. IEEE/ION Position Location Navigat. Symp. (PLANS)*, May 2010, pp. 598–612.
- [16] *Compact, Precision Ten Degrees of Freedom Inertial Sensor ADIS16448*, Analog Devices, Cambridge, MA, USA, 2014.
- [17] J. L. Crassidis, "Sigma-point Kalman filtering for integrated GPS and inertial navigation," *IEEE Trans. Aerosp. Electron. Syst.*, vol. 42, no. 2, pp. 750–756, Apr. 2006.
- [18] N. Trawny and S. I. Roumeliotis, "Indirect Kalman filter for 3D attitude estimation," Dept. Comput. Sci. Eng., Univ. Minnesota, Minneapolis, MN, USA, Tech. Rep., 2005.
- [19] J. A. Hesck, D. Kottas, S. L. Bowman, and S. I. Roumeliotis, "Consistency analysis and improvement of vision-aided inertial navigation," *IEEE Trans. Robot.*, vol. 30, no. 1, pp. 158–176, Feb. 2014.
- [20] S. Leutenegger, S. Lynen, M. Bosse, R. Siegwart, and P. Furgale, "Keyframe-based visual-inertial odometry using nonlinear optimization," *Int. J. Robot. Res.*, vol. 34, no. 3, pp. 314–334, 2015. [Online]. Available: <http://ijr.sagepub.com/content/34/3/314.abstract>
- [21] *IEEE Standard for Inertial Sensor Terminology*, IEEE Standard 528-2001, 2001.
- [22] N. El-Sheimy, H. Hou, and X. Niu, "Analysis and modeling of inertial sensors using allan variance," *IEEE Trans. Instrum. Meas.*, vol. 57, no. 1, pp. 140–149, Jan. 2008.
- [23] P. D. Abramson, "Simultaneous estimation of the state and noise statistics in linear dynamical systems," Ph.D. dissertation, Dept. Aeronautics Astron., Massachusetts Inst. Technol., Cambridge, MA, USA, 1968.
- [24] R. E. Kalman, "A new approach to linear filtering and prediction problems," *J. Basic Eng.*, vol. 82, no. 1, pp. 35–45, 1960.
- [25] Z. Ghahramani and G. E. Hinton, "Parameter estimation for linear dynamical systems," Dept. Comput. Sci., Univ. Toronto, Toronto, ON, Canada, Tech. Rep. CRG-TR-96-2, 1996.
- [26] R. H. Shumway and D. S. Stoffer, "An approach to time series smoothing and forecasting using the EM algorithm," *J. Time Ser. Anal.*, vol. 3, no. 4, pp. 253–264, 1982.
- [27] N. K. Gupta and R. K. Mehra, "Computational aspects of maximum likelihood estimation and reduction in sensitivity function calculations," *IEEE Trans. Autom. Control*, vol. 19, no. 6, pp. 774–783, Dec. 1974.
- [28] C. Moler and C. Van Loan, "Nineteen dubious ways to compute the exponential of a matrix, twenty-five years later," *SIAM Rev.*, vol. 20, no. 4, pp. 801–836, 1978.
- [29] C. Van Loan, "Computing integrals involving the matrix exponential," *IEEE Trans. Autom. Control*, vol. 23, no. 3, pp. 395–404, Jun. 1978.
- [30] *IEEE Recommended Practice for Inertial Sensor Test Equipment, Instrumentation, Data Acquisition, and Analysis*, IEEE Standard 1554-2005, Nov. 2013, pp. 1–145.
- [31] *BMX055 Data Sheet: Small, Versatile 9-Axis Sensor Module*, Bosch, Stuttgart, Germany, 2014.
- [32] *GG1320AN RLG Data Sheet: Digital Ring Laser Gyroscope*, Honeywell, Morristown, NJ, USA, 2010.
- [33] J. Nikolic et al., "A synchronized visual-inertial sensor system with FPGA pre-processing for accurate real-time SLAM," in *Proc. IEEE Int. Conf. Robot. Autom. (ICRA)*, May/Jun. 2014, pp. 431–437.
- [34] M. Kaess and F. Dellaert, "Covariance recovery from a square root information matrix for data association," *J. Robot. Auto. Syst.*, vol. 57, pp. 1198–1210, Dec. 2009.
- [35] *3-Axis Test System With Thermal Shroud TES-4V33-TG*, Motion Dynamic, La Chaux-de-Fonds, Switzerland, 2013.
- [36] A. Chatfield, *Fundamentals of High Accuracy Inertial Navigation*. Reston, VA, USA: AIAA, 1997.



**Janosch Nikolic** received the B.Sc. degree in electrical engineering from Hochschule für Technik Rapperswil, Rapperswil, Switzerland, and the M.Sc. degree in signal processing and communications from the University of Edinburgh, Edinburgh, U.K. He is currently pursuing the Ph.D. degree with the Autonomous Systems Laboratory, ETH Zurich, Zurich, Switzerland, under Prof. R. Siegwart. His research is focused on the design and calibration of visual-inertial sensor systems with application to localization and mapping, and robot guidance.



on long-term autonomy for robotic systems, including mapping, localization, and planning.

**Paul Furgale** received the Ph.D. degree from the University of Toronto Institute for Aerospace Studie, in 2011, where he developed algorithms to support over the horizon sample return for planetary exploration rovers as part of the Autonomous Space Robotics Laboratory. His Ph.D. work was tested in the Canadian High Arctic and integrated into the Canadian Space Agency rover prototypes. He is currently the Deputy Director of the Autonomous Systems Laboratory with the Swiss Federal Institute of Technology, ETH Zurich. His research is focused



sensory and estimation techniques for navigation of autonomous systems.

**Amir Melzer** received the B.Sc. degree in electrical engineering with a specialization in signal processing and communications from the Holon Institute of Technology, Holon, Israel, and the M.Sc. degree in electrical engineering from Hochschule für Technik Rapperswil, Rapperswil, Switzerland. He is currently with the Autonomous Systems Laboratory, Swiss Federal Institute of Technology, Switzerland, where he is leading the avionic and system design of the solar UAV projects. His research interests include inertial



Technical Activities from 2004 to 2005, a Distinguished Lecturer from 2006 to 2007, and an AdCom member of the IEEE Robotics and Automation Society from 2007 to 2009.

**Roland Siegwart** received the M.Sc. and Ph.D. degrees in mechanical engineering from ETH Zurich, Switzerland. He has been a Professor of Autonomous Systems with ETH Zurich, Switzerland, since 2006, and the Vice President of Research and Corporate Relations since 2010. He leads a large research group working on several aspects of robotics. He is a member of the Swiss Academy of Engineering Sciences and the Officer of the International Federation of Robotics Research. He served as the Vice President of